photonics

MDPI

Article

Core Offset Optical Fiber Sensor Coated with Aluminum-Doped Zinc Oxide for Temperature Measurement

Mario Angel Rico-Mendez [1,2], Romeo de Jesús Selvas-Aguilar [1,*], Ricardo Chapa-Garcia [1], Manuel García-Méndez [1], Juan M. Sierra-Hernandez [3], Norma Patricia Puente-Ramirez [2], Eloisa Gallegos-Arellano [4], Carlos Adrián Calles-Arriaga [5], Arturo Alberto Castillo-Guzmán [1], Leonardo Arévalo [1] and Sheila Bazavilvazo-Azua [1]

[1] Universidad Autónoma de Nuevo León, Facultad de Ciencias Físico-Matemáticas, Av. Universidad S/N, Cd. Universitaria, San Nicolás de los Garza 66455, Nuevo León, Mexico; mricom@uanl.edu.mx (M.A.R.-M.); ricardo.chapagr@uanl.edu.mx (R.C.-G.); manuel.garciamnd@uanl.edu.mx (M.G.-M.); arturo.castillogz@uanl.edu.mx (A.A.C.-G.)
[2] Universidad Autónoma de Nuevo León, Facultad de Ingeniería Mecánica y Eléctrica, Av. Universidad S/N, Cd. Universitaria, San Nicolás de los Garza 66455, Nuevo León, Mexico; norma.puenterm@uanl.edu.mx
[3] Departamento de Ingeniería Electrónica, División de Ingenierías, University of Guanajuato, Carretera Salamanca-Valle de Santiago Km 3.5+1.8, Salamanca 36885, Gto, Mexico; jm.sierrahernandez@ugto.mx
[4] Departamento de Mecatrónica, Universidad Tecnológica de Salamanca, Av. Universidad Tecnológica # 200, Col. Ciudad Bajío, Salamanca 36766, Gto, Mexico; egallegos@utsalamanca.edu.mx
[5] Research and Postgraduate Department, Universidad Politécnica de Victoria, Av. Nuevas Tecnologías 5902, Parque Científico y Tecnológico de Tamaulipas, Ciudad Victoria 87138, Tamaulipas, Mexico; ccallesa@upv.edu.mx
* Correspondence: romeo.selvasag@uanl.edu.mx

Abstract

The design of a temperature sensor employing the Mach–Zehnder configuration with an offset in the fiber core represents a novel methodology that leverages the distinctive attributes of optical fibers to attain enhanced sensitivity and precision in temperature measurement. Ambient temperature measurement is enabled by aluminum-doped zinc oxide (AZO) thin films deposited via sputtering onto optical fiber structures for sensing applications in the 1540–1555 nm wavelength range. This work explores the potential of this interferometer to measure the effective temperature variation within the core offset of an optical fiber in a cost-effective manner.

Keywords: fiber-optic sensor; Mach–Zehnder interferometer; AZO thin films

Check for updates

Received: 16 June 2026
Revised: 15 August 2026
Accepted: 24 August 2026
Published: 7 September 2026

Copyright: © 2026 by the authors. Licensee MDPI, Basel, Switzerland. This article is an open access article distributed under the terms and conditions of the Creative Commons Attribution (CC BY) license.

1. Introduction

Fiber-optic sensors present a versatile solution across a wide spectrum of applications, attributed to their compact design, reduced weight, and cost-effectiveness. Fiber-optic sensors demonstrate a pronounced sensitivity to external physical perturbations, encompassing factors such as temperature [1–3], strain, curvature [4], and torsion [5,6]. In recent decades, fiber optic devices have demonstrated their effectiveness in chemical, physical, and biological sensing. The assessment of ambient temperature is essential for numerous environmental monitoring applications. Fiber-optic measurement systems are consistently proposed to facilitate application-specific quantification of this parameter. Interferometric fiber-optic sensors have been extensively investigated owing to their superior sensitivity to refractive index (RI) changes and their moderate sensitivity to temperature variations. Various configurations of Mach–Zehnder interferometers (MZIs), specifically the core offset

configuration, are employed in their fabrication [7,8], and tapered fiber [9] is used for measurement of temperature and RI [10,11].

Fiber Bragg gratings (FBGs) are a benchmark for temperature sensing, commonly exhibiting wavelength temperature slopes on the order of tens of pm/°C near 1550 nm, with excellent linearity and compact form factors [12,13]. However, practical deployment typically requires inscription (UV or fs) in suitable fibers and, in some cases, packaging strategies to mitigate cross-sensitivities [14,15].

Mach–Zehnder, Sagnac, and Michelson interferometers offer adaptable frameworks to modify sensitivity through geometrical configurations and modal coupling [16,17]. Although they may exceed the performance of bare FBGs in specific configurations, their efficacy is significantly influenced by factors such as fringe visibility and the strength of core–cladding interaction. These factors are, in turn, affected by the choices made during fabrication and the modifications applied to the waveguide [18].

High-index and functional thin films enhance the evanescent field and can enable lossy-mode or plasmonic-like interactions, improving fringe contrast and enabling multi-parameter operation [19–21]. Aluminum-doped zinc oxide (AZO) is a transparent conducting oxide with appealing optical properties in the near-IR and compatibility with scalable deposition [22].

Despite the maturity of FBGs and interferometers, there remains a need for configurations that: (i) are fabricable on standard SMF using minimal equipment; (ii) deliver high-contrast interferometric fringes for robust wavelength demodulation; and (iii) are readily tunable/extendable to multi-parameter sensing through functional coatings.

Moreover, the integration of fiber optic technology with advanced materials, innovative optical structures, and deposition methodologies enables the optical detection of electromagnetic oscillations that arise when the film absorbs light incident upon the surface of the optical fiber [23–25]. Some of the most recently developed sensors are those that are induced when a segment of optical fiber is coated with a thin film, permitting a portion of the wave to propagate through this film. Varying optical properties of the film facilitate the generation of different types of spectra. A critical determinant in the performance of optical fiber sensors is the material used to coat the supporting fiber. The optical properties of the fiber coating material are crucial in defining the characteristics of the sensors [26]. MZI device is well studied, easy to fabricate, and suitable for diverse sensing applications [27–30].

The application of aluminum-doped zinc oxide (AZO) coatings on optical fibers has received significant attention due to their unique, distinctive optical and electrical properties, which can enhance the performance of fiber optic systems. AZO is a transparent conducting oxide (TCO) that combines good electrical conductivity with high optical transparency, making it suitable for various applications, including sensors and photonic devices [31–33].

One of the primary advantages of AZO coatings is their ability to generate lossy mode resonance (LMR) in optical fiber structures. This phenomenon occurs when the optical modes of the fiber interact with the evanescent field of the coated layer, leading to enhanced sensitivity in sensing applications. Prieto-Cortés et al. demonstrated that AZO thin films deposited on multimode optical fibers could effectively generate LMR, which is particularly useful for sensing applications in the 1.55 μm wavelength range, a critical region for telecommunications [34]. Furthermore, the non-toxic characteristics and reduced expenditure associated with AZO, in contrast to alternative materials such as indium tin oxide (ITO), further substantiate its applicability in optical fiber applications [35].

In comparison with intrinsic ZnO, aluminum doping is routinely employed to enhance the free-charge-carrier concentration and thereby decrease the electrical resistivity, while

preserving a high degree of optical transparency. Furthermore, such modifications enable precise tuning of the optical response of the coating through appropriate control of the dopant concentration and the deposition parameters. In the present work, Al was selected because it is an abundant and comparatively low-cost dopant, and because AZO provides an indium-free transparent conducting oxide compatible with RF magnetron sputtering. The deposition process utilized a ceramic target consisting of 98 parts ZnO and 2 parts Al_2O_3, which facilitated the reproducible fabrication of AZO films. Although Ga- and In-doped ZnO are likewise recognized as suitable transparent conducting oxides, these materials were not subjected to experimental evaluation within the scope of this study. Therefore, no claim is made that Al is intrinsically superior to Ga or In for the proposed sensing configuration, and a systematic comparison among ZnO, AZO, GZO, and IZO coatings remains a subject for future work.

The structural characteristics of AZO coatings can be modified through diverse deposition methods, including radio-frequency magnetron sputtering. This method allows for precise control over the thickness and morphology of the AZO films, which directly influence their optical and electrical characteristics. The thickness of the AZO coating can be optimized to improve the confinement and propagation length of optical modes within the fiber [36]. In [37] Walia and Verma reported that the sensitivity of LMR-based tapered fiber optic sensors employing AZO coatings was substantially higher compared to conventional sensors, thereby indicating the potential for enhanced detection capabilities across various applications.

Sensor Operating Principle

An MZI sensor typically comprises both the reference and the sensing arms. A beam splitter, ideally exhibiting a 50/50 splitting ratio, is employed to bifurcate a light beam into two separate paths, which are subsequently recombined by a coupler. The beams, once recombined, engage in interference with each other, resulting in an interference fringe that is contingent upon the optical path difference (OPD) between the two arms. In order to detect or quantify a physical parameter, the reference arm of the MZI remains isolated, while the sensing arm is exposed. The measurement induces alterations in light propagation within the sensing arm, thereby modifying the existing OPD between the two arms.The alteration in the OPD leads to a spectral shift in the interference pattern. An MZI may be fabricated within an optical fiber by dividing the core mode into core and cladding modes and subsequently recombining them into a core mode.

Alterations in the refractive index of the core of an in-fiber MZI over a specific length result in a change in the effective refractive index of the core mode. Consequently, the core undergoes a phase alteration that results in a modification of the OPD between the core and the cladding modes. Variation in the OPD causes a shift in the transmission spectrum, thereby providing a straightforward method to assess the change in the effective refractive index within the core of an optical fiber.

The transmission spectrum is formed by the optical path difference between the core and cladding mode beams, which may be mathematically represented as [38,39]:

$$I = I_{core} + I_{cladd} + 2\sqrt{I_{core} I_{cladd}} \cos(\phi) \quad (1)$$

where I_{core} and I_{clad} denote the intensities of light in the core and cladding modes, respectively. The parameter $\phi = 2\pi\Delta n_{eff} L/\lambda$ represents the phase difference between core and cladding modes, which generates the interference fringe in the transmission. The effective-index difference is defined as $\Delta n_{\text{eff}}(\lambda, T) = n_{\text{eff}}^{\text{core}}(\lambda, T) - n_{\text{eff}}^{\text{clad}}(\lambda, T)$, where $n_{\text{eff}}^{\text{core}}$ and $n_{\text{eff}}^{\text{clad}}$ are the effective refractive indices of the core-guided mode and the cladding mode, respectively (both depend on λ and T). In relation to $\phi = (2m+1)\pi$ in Equation (1), this ad-

dresses the peak of attenuation in m^{th} order. This methodology serves as a straightforward yet efficient means of quantifying index modification within an optical fiber.

The design of a temperature sensor employing the MZI configuration, characterized by an offset within the fiber core, represents a methodology that leverages the distinctive attributes of optical fibers to attain enhanced sensitivity and precision in temperature measurement. This configuration is particularly advantageous due to its inherent ability to detect phase shifts caused by changes in temperature, making it a popular choice for various sensing applications. Zhan et al. in [40] demonstrated that by sandwiching a section of few-mode multicore fibers (FM-MCF) between two single-mode multicore fibers with a rotational offset, this design allows intermodal interference, which enhances the sensitivity to temperature changes while also enabling strain.

The offset creates a differential path length for the light traveling through the fiber, resulting in a phase difference that is sensitive to temperature variations. This principle has been successfully implemented in diverse configurations, notably those incorporating tapered fibers, which can further augment sensitivity [41–43]. When an offset is introduced in the fiber core, it alters the effective refractive index experienced by the light propagating through the fiber. This change can significantly enhance the sensitivity of the sensor to temperature variations. Huerta-Mascotte et al. in [44] demonstrated that a core–offset MZI based on dispersion-shifted fiber could effectively sense torsion, demonstrating the adaptability of this configuration for a wide range of sensing applications. The introduction of an offset facilitates improved mode coupling, consequently enhancing the sensitivity to external stimuli, due to the increased prominence of the differential path length.

Research indicates that AZO thin films are capable of exhibiting significant transparency in the visible and near-infrared spectra while concurrently maintaining low electrical resistance, thereby rendering them suitable for applications where both optical and electrical performances are critical [45]. AZO is known for its excellent thermal stability and resistance to environmental degradation. The stability of AZO is crucial for sensors functioning in challenging environments, as it guarantees consistent performance over prolonged durations. The thermal stability of AZO thin films has been demonstrated in various applications, including solar cells, where preservation of material integrity is essential [46,47].

Temperature variations can induce changes in the refractive index of the fiber material and the surrounding medium, leading to measurable shifts in the optical signals transmitted through the fiber. Ma et al. in [48] emphasized that fluctuations in temperature have a direct impact on the optical path length, resulting in a discernible phase shift within the interference pattern. This shift can be quantitatively evaluated to ascertain the change in temperature. The optical properties of the fiber, including its refractive index, are temperature–dependent. With an increase in temperature, the refractive index of materials tends to decrease, potentially causing a shift in the wavelength of light propagating through the optical fiber.

We propose a core–offset in fiber MZI functionalized with an Al–doped ZnO (AZO) thin film. Combining controlled core offsets with a transparent conducting oxide provides three practical advantages: stronger core–cladding coupling and higher fringe visibility, which improves wavelength demodulation robustness; fabrication on standard single-mode fiber with only fusion-splice offsets plus one sputtering step (no inscription, etching, or tapering), enabling low cost and scalability; and functional-coating tunability and extensibility to dual-parameter sensing. Experimentally, the device exhibits a linear temperature response of $\sim$45 pm $^{\circ}C^{-1}$ with $R^2 > 0.99$ near 1547 nm. Finite-Difference Time-Domain (FDTD) simulations corroborate the AZO-induced enhancement of multimode interference and explain the observed improvement in fringe contrast.

For this purpose, we prepared an optical sensor based on an optical fiber system coated with an AZO film, deposited by the RF sputtering technique. The fiber sensor operates based on the response of AZO coated fiber structures within the near-infrared spectrum, specifically identified as the C-band wavelength range, approximately between 1525 nm and 1565 nm, with a central wavelength at ≈1550 nm.

At room temperature, ZnO exhibits a direct band gap of $E_g \approx 3.37$ eV (near-band-edge absorption at ∼368 nm) [49,50]. In Al-doped ZnO (AZO), the apparent optical gap typically lies in the ∼3.3–3.6 eV range, varying with Al content and free-carrier density [51–53].

In the longer wavelength region, at the threshold of the infrared (IR) range (from 900–2500 nm), the material exhibits lattice vibrations (phonons). The phonons are coupled with plasmons, which are produced by the conduction electrons within the ZnO lattice, along with the additional electrons supplied by aluminum. Therefore, absorption is anticipated in this region, with a bulk plasma frequency w_p approximately 1500 nm for AZO, as described in a previous work [34].

This work demonstrates and analyzes a standard-SMF core-offset MZI with an AZO thin-film coating for temperature sensing in the 20–100 °C range. We fabricate AZO-coated heads with three 30 µm offsets, reporting wavelength-based calibration (sensitivity near 1547 nm), linearity, resolution, and repeatability to 10 °C steps. We support the experiments with a 2D FDTD model that reproduces core–cladding coupling in the offset sections. Finally, we quantify fringe visibility changes due to AZO and discuss application context and biochemical compatibility to clarify practical deployment.

2. Materials and Methods

As the first step for sensor fabrication, a thin film of AZO was deposited onto the optical fibers. Previously, optical fibers were mounted on glass substrates attached with a special vacuum scotch tape. Bare sections of substrate were then used to characterize films with UV-Vis spectroscopy through transmittance measurements. Several experiments were performed to ensure the fibers were totally coated with the AZO film. For this aim, optical microscopy images were obtained for visual testing of the coated fibers.

With fibers attached to substrates, AZO films were deposited by RF magnetron sputtering (using a TE –12P intercovamex system, equipped with an RF power source). A circular ceramic target with a diameter of 1 and a thickness of 1/8 in was utilized, composed of a powder mixture consisting of 98 parts ZnO and 2 parts Al_2O_3. Subsequently, the substrate was secured on the holder in a position parallel to the target, maintaining a separation of 5 cm. The deposition processes were implemented within a bell-jar glass chamber, which sustained a base pressure of 7.0×10^{-5} Torr. The sputtering process was executed at a working pressure of 60 mTorr, with an argon flow rate of 20 sccm, which was regulated by an electronic mass flow meter. Plasma was generated by applying an RF power of 80 W. Before initiating the deposition, the target underwent a presputtering procedure for a duration of 5 min, aimed at eliminating any contaminants. The deposition duration was 5 min, and no deliberate substrate heating was applied. The AZO film thickness was assessed ex situ using Filmetrics on a planar witness substrate coated simultaneously with the optical fibers. The reported optical thickness of approximately 50 nm therefore corresponds to the planar substrate and not to a direct cross-sectional measurement of the coating deposited on the curved fiber surface [54]. SEM and EDX characterization could not be performed because the required instrumentation was not available. Consequently, comprehensive characterization of the film morphology, elemental distribution, local Al concentration, and coating uniformity is not included within the scope of the present study.

The selected fabrication parameters were chosen to provide a reproducible compromise between cladding-mode excitation, insertion loss, and coating-induced evanescent

interaction. A lateral core offset of 30 µm was used because this value promotes efficient coupling from the core mode to cladding modes while maintaining manageable optical losses in fusion-spliced core-offset MZI structures. The AZO thickness of approximately 50 nm was selected as a practical trade-off: it is sufficiently thin to avoid excessive attenuation while still modifying the cladding-mode boundary condition and enhancing the interaction with the evanescent field. Reproducibility was addressed by keeping constant the sputtering parameters, deposition time, offset distance, and fusion-splicing conditions. The AZO-related improvement is therefore quantified not only through qualitative field redistribution, but also through the increased fringe visibility/notch contrast and the modified simulated spectral response around the 1547 nm operating wavelength.

After deposition, parts of the substrate were analyzed with a UV–Vis spectrophotometer (Thermo Scientific Evolution 600, Thermo Electron Scientific Instruments LLC, Madison, WI, USA). in the wavelength range of 300 to 900 nm. Through transmittance curves, the band gap was extracted by Tauc curves, where a band gap of $E_g = 3.36$ eV was obtained, corresponding to the value reported for AZO.

2.1. Sensor Fabrication

A Corning SMF-28e single-mode fiber (Corning Incorporated, Corning, NY, USA) was used to fabricate the MZI. The core diameter was 8 µm, and the cladding diameter was 125 µm. Then, two segments (A and D segments) of SMF with a length of 200 mm were spliced without any core offset to one of the fiber connectors using a commercial splicer (FITEL, arc S178 ver.2), as presented in Figure 1. Following this procedure, a single-mode fiber segment with a core offset of 30 µm was subsequently spliced to the earlier connected SMF (B segment), extending it by two centimeters. Then another identical-length segment (C segment) was spliced with a 30 µm-core offset. Ultimately, a splice was performed using a core offset of 30 µm, resulting in a final segment D length of 200 mm for the FC/UPC connectors.

We adopted a lateral core offset of 30 µm at each splice because this value is widely reported to yield robust cladding-mode excitation in core-offset MZIs fabricated by standard fusion splicing. In particular, Huerta-Mascotte et al. implemented a 30 µm offset in a core-offset interferometer, and several studies scanning offset distances report the expected trade-off, selecting an intermediate value for best fringe visibility vs. insertion loss [55,56].

Figure 1 illustrates that at the initial core-offset splice, the energy propagating in the fundamental core mode is coupled into both the core and cladding of the subsequent SMF section. Given that the cladding of the SMF possesses an effective refractive index lower than that of the core, a phase difference between the core and cladding modes is accrued at the second splice. This accrued phase difference then propagates through the core, and this sequence of events recurs up to the third splice.

At least two spatially separated offset junctions are required to implement an in-line core–cladding Mach–Zehnder interferometer. The first offset junction couples the fundamental core mode into a combination of core and cladding modes. These modes accumulate a relative phase difference while propagating through the intermediate fiber section, and a subsequent offset junction recouples part of the cladding-mode energy into the core, producing the measurable interference spectrum. In contrast, a single isolated offset would primarily behave as a mode converter and loss-producing discontinuity, without providing a well-defined second coupling region for modal recombination. The present device contains three 30 µm offset junctions at the A–B, B–C, and C–D interfaces. The third junction reinforces modal recoupling and improves the visibility of the spectral feature used for temperature tracking. This enhancement is achieved at the cost of increased

insertion loss; consequently, the chosen offset constitutes an optimized trade-off among cladding-mode excitation, interference visibility, and the level of transmitted optical power.

The offset disrupts the fiber symmetry, allowing part of the light to couple into the cladding. The resultant structure is composed of four distinct segments (A–D), where the core-offset regions function as beam splitters and combiners. This approach obviates the need for intricate fabrication techniques, such as tapering or chemical etching, while ensuring precise control over mode coupling.

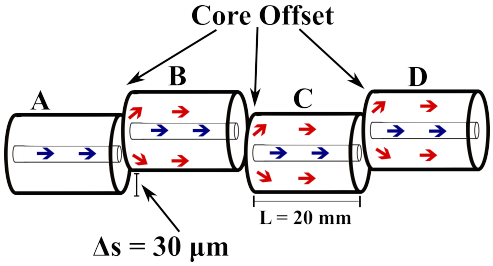


Figure 1. Schematic of the sensor cutting and splicing process. Sections A–D denote the SMF-28e fiber segments; A and D are 200 mm long, whereas B and C are 20 mm long. The blue arrows represent light propagating in the core mode, while the red arrows represent light coupled into cladding modes at the core-offset splice junctions. The black arrows labeled "Core Offset" indicate the lateral misalignment between adjacent fiber sections. $\Delta s = 30$ µm denotes the lateral core offset, and $L = 20$ mm denotes the length of each intermediate fiber section B and C.

The field distributions reported in the numerical analysis are normalized and are intended solely to illustrate the qualitative redistribution of modal energy; they do not correspond to, nor should they be interpreted as, an integrated core-to-cladding power ratio. The insertion loss of the fabricated structure was not independently measured relative to a straight-SMF reference under identical conditions. Therefore, the absolute power recorded by the OSA should not be interpreted as the insertion loss of the interferometer. A fully calibrated insertion-loss characterization is required to quantitatively assess the optical penalty induced by the three lateral offset junctions and the AZO (Al-doped ZnO) coating.

Throughout the process of managing and assembling the in-line interferometer, it became imperative to operate the splicer in manual mode due to its inability to detect fibers with cladding diameters measuring 80 µm or less. As illustrated in Figure 2a, the two SMF cores were first aligned and subsequently displaced laterally by 30 µm. This controlled misalignment is essential for generating reproducible cladding mode excitation.

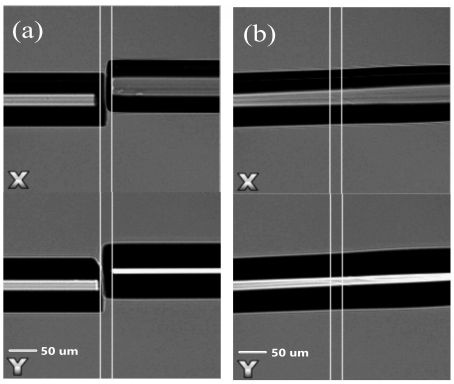


Figure 2. Fusion-splicing procedure used to produce the 30 µm lateral core offset. (**a**) Alignment of the two SMF-28e fiber sections before introducing the controlled 30 µm lateral displacement; (**b**) resulting core-offset splice after applying three arc discharges to join the misaligned fiber sections. The splicer parameters were: arc power = 100, pre-fusion time = 160 ms, arc duration = 750 ms, and cleaning time = 200 ms.

Figure 2b illustrates the result of administering three discharges, which constitute the requisite number of discharges to achieve the union of both cores, as a result of dimensional misalignment. A pair of short SMF stubs was inserted between the lead-in and lead-out SMFs, resulting in a minor core misalignment. The consistency and reliability of this process were validated through numerous trials, highlighting its appropriateness for the scalable production of sensors.

To characterize the sensor assembly, the light produced by the EDF-based source was propagated through the core-offset structure, and the resulting output power spectrum was measured using an Anritsu MS9740A optical spectrum analyzer (Anritsu Corporation, Atsugi, Kanagawa, Japan) with a nominal wavelength resolution of 0.03 nm. Figure 3 presents the absolute output spectrum measured by the OSA and not the normalized transfer function of the passive interferometer. The measured spectrum contains the combined contributions of the source spectral profile and the wavelength-dependent transmission of the core-offset structure. A dominant output feature was observed near 1547 nm and was subsequently monitored during the temperature experiments.

This spectrum constitutes a baseline for assessing the effects of temperature and AZO coating on the sensor performance.

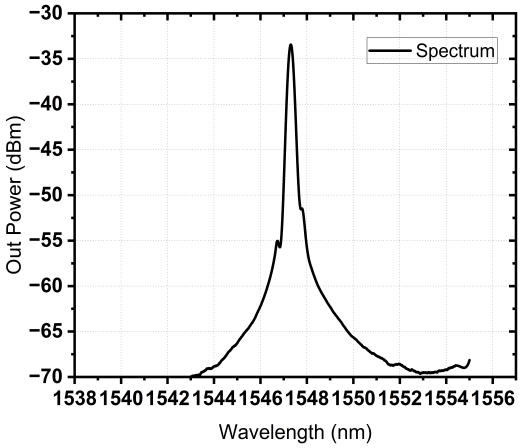


Figure 3. Absolute output power spectrum measured after the core-offset sensor at the initial temperature.

Figure 4 illustrates the interferometer, incorporating a metal coating of zinc oxide doped with aluminum, which exhibits a high refractive index (n_{AZO} = 1.524 at 1550 nm). This coating, deposited via magnetron sputtering, enhances the effective refractive index contrast (Δn_{eff}) between the core and cladding, thereby facilitating a redistribution of cladding modes and energy towards the aluminum coating [57,58]. This phenomenon is accompanied by an augmentation in the difference of the effective refractive index, redistributing cladding mode energy toward the AZO layer, as its high refractive index strengthens the evanescent field interaction, leading to reduced fringe separation ($\Delta\lambda$). The sharp transmission peak observed at approximately 1547 nm does not correspond to a single resonance of the MZI itself. Instead, it originates from the spectral tuning between the erbium-doped fiber (EDF) laser emission and the transmission maximum of the core-offset MZI filter. It is pertinent to note that optimal visibility is achieved when the intensities of the interfering modes are equivalent. In the present scenario, the redistribution of energy towards the cladding modes results in an elevated visibility of the interference spectrum [59].

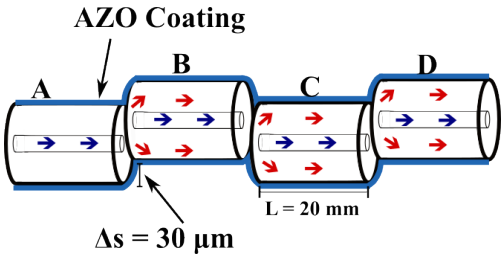


Figure 4. Schematic of the core-offset MZI after AZO coating. Sections A–D denote the four SMF-28e fiber segments. The blue outer layer represents the AZO coating deposited on the fiber surface. The blue arrows indicate light propagation predominantly in the core mode, whereas the red arrows represent light coupled into cladding modes after the core-offset splice junctions. The lateral core displacement at each junction is $\Delta s = 30$ μm. Sections B and C are the intermediate interferometric sections, each with a length of $L = 20$ mm.

2.2. Temperature Sensor

The thermal response of the proposed sensor is evaluated by positioning the metal beam, which houses the interferometer, on a heating plate maintained at an ambient temperature of 20 °C. The variation in phase difference resulting from the temperature of fiber can be expressed by Equation (2), where the temperature fluctuations can be demonstrated as

$$\Delta(\Delta\phi) = \frac{2\pi}{\lambda} L \Delta T \left[\Delta\eta_{eff}\alpha + \left(\eta_{co} n_{eff}^{core} - \eta_{clad} n_{eff}^{clad} \right) \right] \quad (2)$$

where η_{co} and η_{clad} denote the thermo-optic coefficients of the core and cladding, respectively, and α represents the thermal expansion coefficient. The observed spectral shift arises from the temperature dependence of the effective-index difference between the core and cladding-guided modes, $\Delta n_{\mathrm{eff}} = n_{\mathrm{eff}}^{\mathrm{core}} - n_{\mathrm{eff}}^{\mathrm{clad}}$, rather than from the core index alone. The phase change is Equation (2), where α is the thermal expansion coefficient and $\eta_{co} n_{eff}^{core}$, $\eta_{clad} n_{eff}^{clad}$ are the effective thermo-optic coefficients of the core and cladding modes, respectively. The AZO coating modifies $n_{\mathrm{eff}}^{\mathrm{clad}}$ (and thus $\eta_{clad} n_{eff}^{clad}$) through the evanescent field interaction at the fiber/film/air interface.

2.3. Numerical Simulation by FDTD

AZO complex refractive index ($n + ik$) in the 1.54–1.555 μm window was taken from the literature, using a Drude–Lorentz fit derived from spectroscopic ellipsometry. We used the parameterized model reported by Riley et al. [60], evaluated at our wavelengths, and employed it directly in the FDTD material model. Trends and magnitude were cross-checked against near-IR data from Naik et al.[61] and against DC-sputtered AZO measured by Guillén et al. [62] up to 2100 nm, which encompasses the telecom band. The resulting $n(\lambda)$ and $k(\lambda)$ used in simulation are plotted in Figure 5.

To enhance the experimental findings, a numerical analysis of the electromagnetic propagation within the offset-core Mach–Zehnder interferometer was conducted by employing the FDTD method. The computational domain was delineated by a dielectric matrix denoted as ER with dimensions measuring 173 × 2552, indicative of a cross-sectional representation of the optical fiber encompassed within an air region. Figure 6 delineates the ER matrix constructed to represent the optical fiber configuration, wherein the geometry of the fiber is distinctly characterized by a core diameter of 8 μm and a cladding diameter of 125 μm. The fiber's overall length measures 50 mm and is partitioned into four discrete sections: A (5 mm), B (20 mm), C (20 mm), and D (5 mm). A lateral offset of 30 μm was incorporated at each splice junction (A–B, B–C, C–D), emulating the procedures employed during the experimental fabrication process.

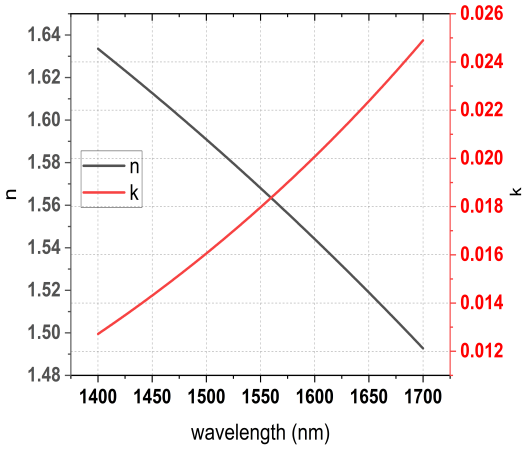


Figure 5. Literature-derived optical constants of AZO. Refractive index $n(\lambda)$ and extinction coefficient $k(\lambda)$ from 1.4–1.7 µm, highlighting the 1540–1555 nm band used in this work.

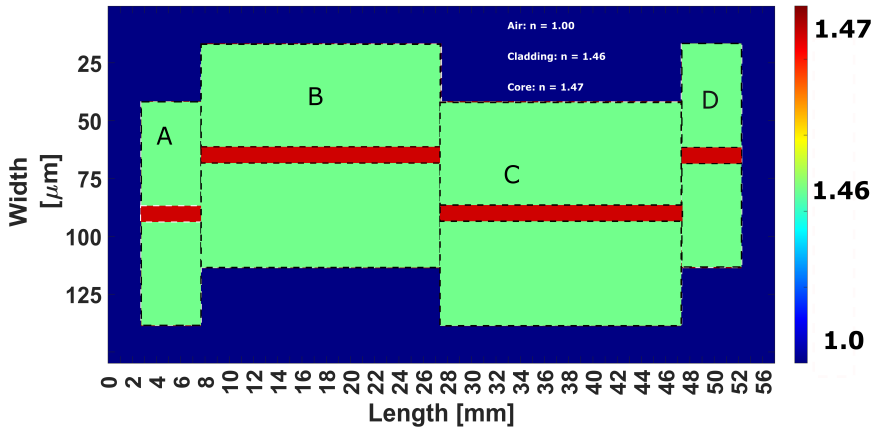


Figure 6. Refractive-index distribution (ER matrix) used in the FDTD simulation. The blue region represents the surrounding air ($n = 1.00$), the orange/red region represents the silica cladding ($n = 1.46$), and the central high-index region represents the fiber core ($n = 1.47$). Sections A–D denote the four fiber segments with lengths of 5, 20, 20, and 5 mm, respectively. The core diameter is 8 µm and the cladding diameter is 125 µm. A lateral core offset of 30 µm is introduced at the A–B, B–C, and C–D junctions.

The refractive indices were set to 1.47 for the core and 1.46 for the cladding. To ensure numerical stability, spatial discretization intervals of $\Delta x = \Delta y = 1.0884 \times 10^{-7}$ m were employed in accordance with the Courant condition. To enhance computational efficiency, the ER matrix was reduced by a factor of 10. Absorbing boundary conditions were applied through the implementation of Perfectly Matched Layers (PMLs) to minimize unphysical reflections. The simulation domain thus corresponds to ∼32,000 wavelengths z at 1550 nm. Time stepping uses $\Delta t = \Delta x/(2c) \approx 1.8 \times 10^{-16}$ s, and runs continue until field decay ensures convergence (energy in the domain $< 10^{-5}$ of the source after steady state). Perfectly matched layer (PML) boundaries are applied on all sides with a thickness of 16 cells and polynomial grading of order 3 to suppress reflections below −50 dB. Material dispersion of silica and AZO is introduced via frequency-dependent refractive indices. Splices and offsets are modeled geometrically by lateral displacements of the core region across junction planes, consistent with the 30 µm offsets implemented experimentally. The excitation source is a Gaussian-modulated sinusoidal plane wave $E_{\mathrm{src}}(y,t) = E_0 \exp\left[-\frac{(y-y_0)^2}{\sigma^2}\right] \sin(2\pi f t)$, launched at one fiber end, and transmission is monitored along z.

This approach entails the discretization of Maxwell's curl equations across both temporal and spatial dimensions, leading to the derivation of update equations for the magnetic field components H_x and H_y, and the electric field component E_z. The subsequent relations were utilized in the simulations:

$$H_y\Big|_{i,j+\frac{1}{2}}^{n+\frac{1}{2}} = H_y\Big|_{i,j-\frac{1}{2}}^{n-\frac{1}{2}} - \frac{\Delta t}{\mu_0}\left(\frac{E_z|_{i,j+1}^{n} - E_z|_{i,j}^{n}}{\Delta}\right) \tag{3}$$

$$H_x\Big|_{i+\frac{1}{2},j}^{n+\frac{1}{2}} = H_x\Big|_{i-\frac{1}{2},j}^{n-\frac{1}{2}} - \frac{\Delta t}{\mu_0}\left(\frac{E_z|_{i,j+1}^{n} - E_z|_{i,j}^{n}}{\Delta}\right) \tag{4}$$

$$E_z|_{i,j}^{n+1} = E_z|_{i,j}^{n} + \frac{\Delta t}{\varepsilon_0}\left(\frac{H_x|_{i+\frac{1}{2},j}^{n+\frac{1}{2}} - H_x|_{i-\frac{1}{2},j}^{n+\frac{1}{2}}}{\Delta} - \frac{H_y|_{i,j+\frac{1}{2}}^{n+\frac{1}{2}} - H_y|_{i,j-\frac{1}{2}}^{n+\frac{1}{2}}}{\Delta}\right) \tag{5}$$

Simulations were carried out over a spectral range spanning from 1540 nm to 1555 nm, aligning with the band region employed in experimental procedures. Radial field distributions were further analyzed at fiber positions of 4 mm, 9 mm, 23 mm, 26 mm, 40 mm, and 45 mm, corresponding to regions within sections A, B, C, and D. These results reveal the spatial redistribution of energy caused by the 30 µm offsets, confirming the role of misalignment in enhancing the multimodal interference.

The FDTD map (Figure 7) illustrates that the majority of the energy is predominantly confined within the core along sections A–D, exhibiting only moderate leakage into the cladding at the 30 µm offset junctions. The radial intensity profiles at 4 mm and 9 mm demonstrate the presence of weak side lobes, which suggest a limited mode conversion. At 23 mm and 26 mm, situated within and after the second offset, respectively, the coupling is observed to increase, yet it rapidly diminishes as it approaches the cladding. By 40 mm and 45 mm the interference is visible yet comparatively low-contrast, consistent with weaker cladding-mode participation.

Introducing the AZO coating (Figure 8) increases the effective index contrast. This enhancement boosts evanescent interaction and cladding-mode excitation. The electric field distribution E_z exhibits a more distinct appearance of fringe bands subsequent to each offset, while the radial cuts at intervals of 4, 9, 23, 26, 40, and 45 mm present broader and more elevated peaks extending into the cladding. This stronger multimode interaction yields higher fringe visibility and a more pronounced longitudinal oscillation of intensity.

To elucidate the role of the AZO film, we performed side-by-side FDTD simulations at the experimental operating wavelength (1547 nm) for uncoated and AZO-coated configurations. The ER index map and Yee-grid settings follow Section 2.3. In the coated case, the higher index contrast at the cladding interface increases cladding-mode participation after each offset (A–B, B–C, C–D), thereby enhancing multimode interference and fringe visibility.

At a wavelength of 1547 nm, both structures demonstrate offset-induced mode coupling; however, the uncoated fiber confines the field more effectively, resulting in fringes of lower contrast and diminished excitation of the cladding. The fiber coated with AZO exhibits more pronounced redistribution of energy into the cladding at all sampled positions, especially subsequent to the A–B and B–C transitions, leading to more distinct interference fringes and heightened notch contrast, as evidenced in Table 1. Overall, AZO acts as a functional layer that amplifies multimode coupling at the operating wavelength where the device is experimentally most responsive.

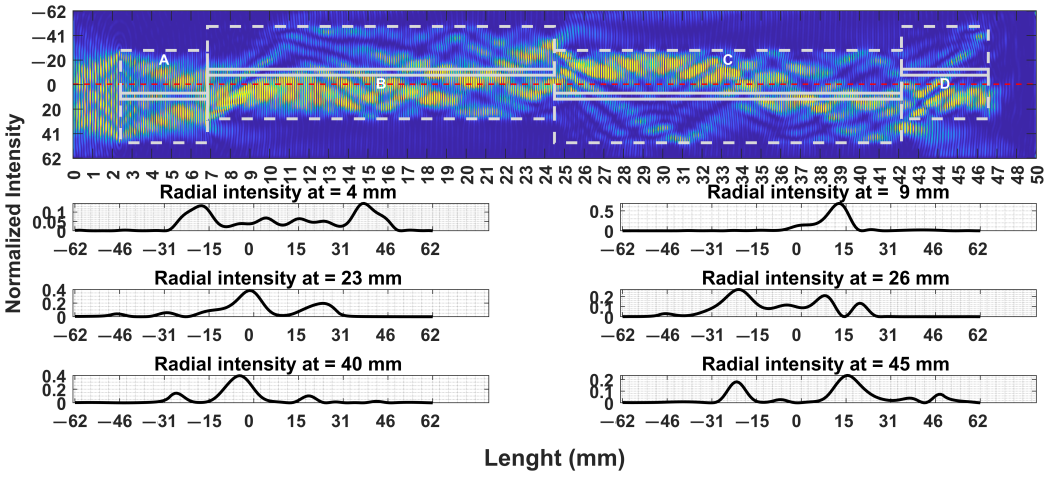


Figure 7. Field propagation and radial intensity profiles at $\lambda = 1554$ nm for the offset-core fiber **without AZO coating**. Sections A–D denote the four fiber segments used in the FDTD model: A and D are 5 mm long, whereas B and C are 20 mm long. The lateral displacement between consecutive sections represents the 30 μm core offset introduced at the A–B, B–C, and C–D junctions. The dashed line indicates the outer boundary of the fiber/cladding geometry. The color map represents the normalized electric-field intensity: blue corresponds to lower intensity, cyan and green to intermediate intensity, and yellow to red to progressively higher intensity. The radial intensity profiles shown below the propagation map correspond to positions of 4, 9, 23, 26, 40, and 45 mm along the fiber. The field remains predominantly confined near the core, with comparatively weak coupling into the cladding, resulting in lower-contrast multimode interference.

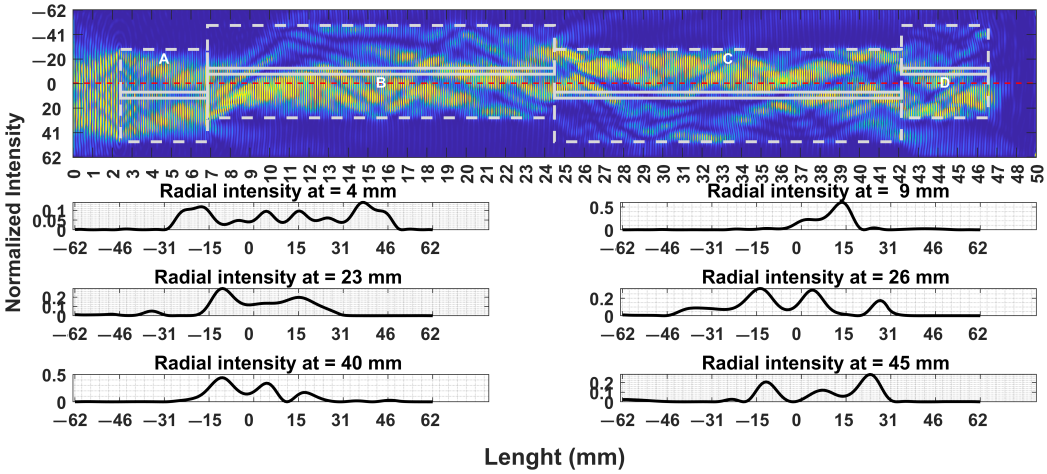


Figure 8. Field propagation and radial intensities at $\lambda = 1554$ nm for the offset-core fiber **with AZO coating**. The AZO layer increases the refractive index contrast, enhancing cladding mode excitation and generating stronger multimodal interference.

Figure 9 presents the numerically calculated transmission spectra of the passive core-offset MZI within the 1540–1555 nm wavelength range, enabling a comparison between the uncoated structure and the configuration incorporating an AZO coating. The two spectra display a quasi-periodic interferometric response that is characteristic of multimode core–cladding coupling induced by the applied lateral offsets. Analysis of the simulated transmission spectrum in the vicinity of 1550 nm indicates that the free spectral range (FSR) can be determined from the wavelength separation between consecutive transmission maxima, yielding an average value in the range of approximately 3.5–3.7 nm. The AZO layer modifies the effective refractive index of the cladding-guided fields and slightly alters the spectral shape, consistent with the expected perturbation of the cladding-mode contribution to the interference.

Table 1. Qualitative comparison at $\lambda = 1547$ nm between the simulated optical-field the offset-core fiber without AZO and with AZO coating.

Aspect	Without AZO	With AZO Coating
Mode confinement	Mostly confined in the core; limited leakage to cladding	Stronger energy redistribution into the cladding due to higher index contrast.
Cladding-mode excitation	Moderate at offsets; decays rapidly	Enhanced after each offset; sustained along sections B–C
Interference visibility/contrast	Lower-contrast fringes; weaker notches	Higher-contrast fringes; deeper, sharper notches
Fringe spacing (qualitative)	Larger spacing (fewer fringes in window)	Slightly reduced spacing (more fringes) from increased Δn_{eff}
Radial profiles (cuts at 4, 9, 23, 26, 40, 45 mm)	Narrow peaks centered at core; small side-lobes	Broader peaks extending into cladding; pronounced side-lobes
Operating point near 1547 nm	Moderate response around spectral peak	Enhanced response aligned with experimental peak at 1547 nm
Short-term stability (qual.)	Comparable	Comparable; AZO does not degrade short-term stability

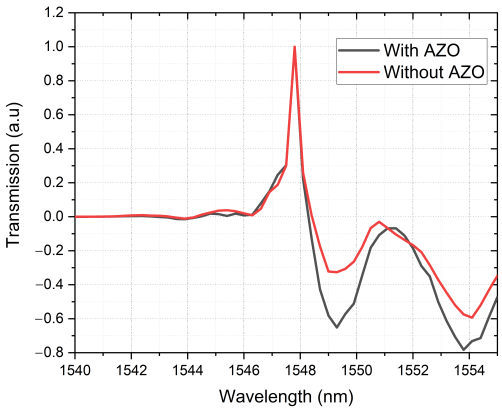


Figure 9. Simulated transmission spectra of the passive core-offset Mach–Zehnder interferometer in the 1540–1555 nm wavelength range, comparing configurations with and without the AZO coating. The fringe spacing in the vicinity of 1550 nm FSR is determined from the spectral separation between adjacent transmission maxima and is found to be approximately 3.5–3.7 nm.

2.4. Experimental Setup

Figure 10 illustrates the experimental configuration employed to evaluate the MZI under varying temperature conditions. The system's source comprised a semiconductor laser (Qphotonics, model QFBGLD-908-150J) utilized for pumping, which was interfaced with a wavelength division multiplexer (WDM). A broadband source was achieved by interfacing the WDM with a 3.5-m segment of EDF (Thorlabs model M5-980-125), which functioned as an active medium to produce a spectrum spanning from 1450 nm to 1650 nm. Subsequently, the output terminal of the erbium-doped fiber (EDF) was interfaced with the MZI, and the opposite end of the interferometer was coupled to an OSA. The MZI maintained thermal contact with a temperature-controlled platform, which comprised a Peltier cell in conjunction with a proportional-integral-derivative (PID) controller, facilitating operation within a temperature range of 0 to 100 °C.

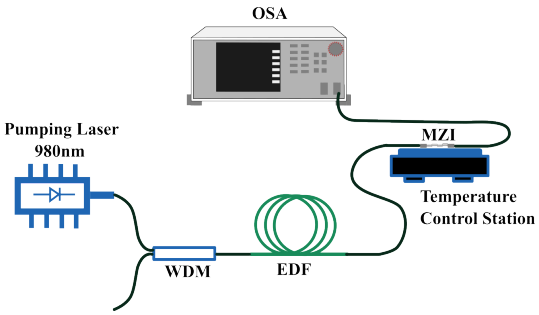


Figure 10. The temperature-controlled setup. A WDM and a 3.5-m EDF provide a broadband source (1450–1650 nm). The interferometer output is measured with an OSA. A PID-controlled Peltier stage applies steps of $\Delta T = 10\,^{\circ}\mathrm{C}$ around the operating point.

A PID Peltier stage applied square steps of $\Delta T = 10\,^{\circ}\mathrm{C}$ around the operating point. The laser was biased at the wavelength λ_q (near 1547 nm) and the transmitted power was recorded with a photodetector (sampling ≥ 1 kHz). Each transition was fitted to a first-order model $y(t) = y_\infty - (y_\infty - y_0)\exp[-(t - t_0)/\tau]$ to obtain the $1/e$ time constant τ and the 10–90% rise/fall times; the corresponding bandwidth estimate is $f_c \approx 1/(2\pi\tau)$.

Temperature was cycled between 20° and 100° using a PID-controlled stage (setpoint tolerance ±0.1°). Unless otherwise stated, measurements were taken in 5 ° steps with a dwell time of 5 min per step to ensure thermal equilibrium before spectral acquisition. Each spectrum is the average of 5–10 traces. Peak tracking near the operating wavelength (∼1547 nm) was performed via centroid/peak fitting. Three full heating–cooling cycles (20→100→20 °) were recorded to evaluate short-term stability, repeatability across cycles, and thermal hysteresis. Optical power at the detector was monitored concurrently to track source fluctuations.

The temperature characterization was repeated over three complete heating–cooling cycles from 20 to 100 °C and back to 20 °C. For the repeatability analysis, the wavelength and optical-power results at each temperature were calculated as the mean of the three independent thermal cycles.

3. Experimental Results and Discussion

Considering variables such as temperature, both the refractive index and the thermal expansion of the material are subject to variability, thereby modifying the optical path length and consequently influencing the interference pattern, as illustrated in Figure 11.

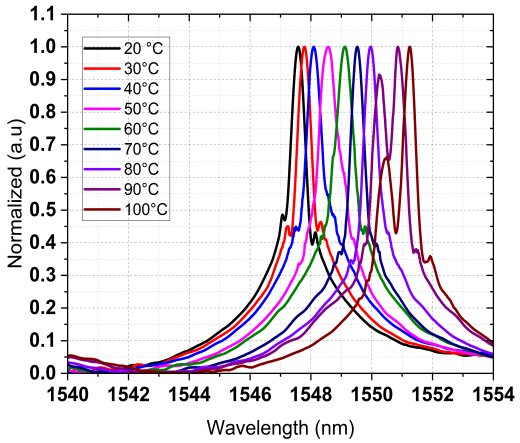


Figure 11. Analysis of the transmission spectra and wavelength shifts of MZI sensor at varying temperatures.

Applying a coating of metal with a high refractive index, such as aluminum and zinc (n_{AZO} = 1.524 at 1550 nm), to the sensor head elevates the energy of the cladding modes, thereby enhancing the visibility of the interference pattern.

The heightened sensitivity to temperature variations can be attributed to the synergistic influence of the thermal expansion and thermo-optical characteristics inherent in both AZO and the fiberglass materials [41].

The temperature assessment was conducted over a range from 20 °C to 100 °C, with increments of 10 °C. To guarantee the integrity of the data, it is imperative that the temperature control system maintains a stable value at each designated set point prior to recording the spectrum. The most prominent peak, originally centered at 1547.7 nm, exhibits the greatest shift of approximately 3.60 nm within the entire interference pattern (refer to the of Figure 12), although this results in a constrained temperature sensitivity of approximately 45 pm/°C ($R^2 > 0.99$). This phenomenon is attributed to the thermo-optic effect observed within the germanium-doped core, which possesses a thermo-optic coefficient higher thermal that of the silica cladding (dn/dT). The linearity confirms the sensor's reliability for quantitative temperature monitoring.

The results indicate that the primary demonstrated contribution of the AZO coating is the enhancement of cladding-mode participation, fringe visibility, and spectral contrast, thereby enabling more robust and reliable tracking of the dominant spectral feature. Although the AZO-coated device exhibited a temperature sensitivity of approximately 45 pm/°C, a nominally identical uncoated device was not subjected to experimental calibration over the corresponding temperature range, precluding a direct quantitative comparison. Therefore, the present results do not establish a quantitative enhancement in temperature sensitivity relative to the uncoated configuration. The comparison between coated and uncoated structures presented in Figures 7–9 is currently restricted to the analysis of simulated field distributions, multimode coupling behavior, and spectral responses. A rigorously controlled experimental investigation directly comparing the temperature sensitivities of coated versus uncoated devices is still required.

Figure 11 shows the measured spectra, each normalized to its respective maximum peak amplitude, in order to emphasize the wavelength drift as a function of temperature. The position of the dominant spectral feature (defined as the maximum of each normalized trace) is indicated to illustrate the systematic rightward shift toward longer wavelengths with increasing temperature. Conversely, Figure 12 presents the quantitative temperature calibration obtained by monitoring the same dominant peak within a fixed spectral window, centered at approximately 1547 nm, for all investigated temperatures.

The free spectral range (FSR) near λ_0 was estimated exclusively from the simulated passive transmission spectrum shown in Figure 9. Under passive conditions, the MZI exhibits a quasi-periodic interference pattern with adjacent fringes separated by approximately 3.5–3.7 nm around 1550 nm, consistent with the reported FSR = 3.6 nm. During laser-assisted operation, only one dominant spectral peak remains, as neighboring fringes are suppressed by the EDF gain profile. Across 20–100 °C the total wavelength excursion is $\Delta\lambda \approx S_T \Delta T \approx 0.045$ nm/°C × 80 °C , which is $<$ FSR; therefore, the tracked fringe does not change order. Each acquisition is validated by checking that the two neighboring peaks (P_{-1}, P_{+1}) retain their relative indices and by a spectrum correlation test to prevent peak swapping under minor power drifts.

The apparent splitting of the main spectral peak at 100 °C does not indicate a stability issue of the interferometer. This transient double feature arises from the bimodal lasing behavior of the EDF source combined with minor thermo-optic birefringence in the AZO-coated fiber at elevated temperature. The phenomenon is reproducible and does not affect

wavelength repeatability or power stability, as confirmed by the one-hour stability test shown in Figure 13.

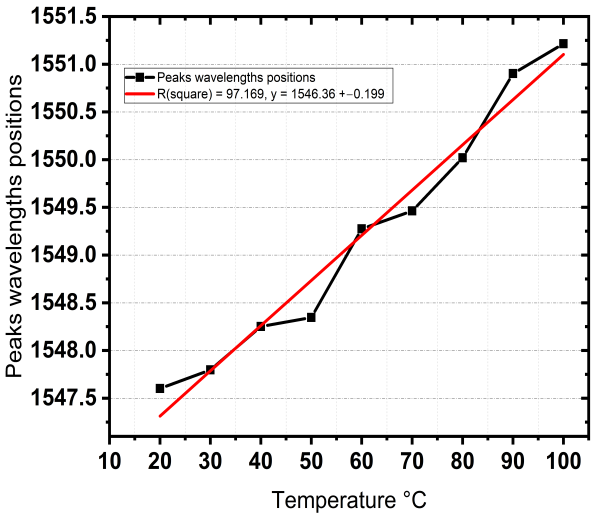


Figure 12. The position of MZI sensor wavelength peaks undergoes shifts at different temperature levels. Peak wavelength (λ_{peak}) is obtained after linear baseline removal by applying a Savitzky–Golay pre-filter and centroid/Lorentzian fitting within a 0.3–0.5 nm window. Given the OSA RBW (0.03 nm) and sampling, the uncertainty is ±(0.02–0.03) nm.

Elevating the temperature results in an augmentation of the effective refractive index for both the cladding modes and the core mode. Nevertheless, due to the germanium doping imparting a higher thermo-optic coefficient to the core, the core mode exhibits a greater change in effective refractive index compared to the cladding modes [63,64].

The stability of the coated MZI was evaluated over the course of one hour by recording the interference pattern of the sensor at room temperature at five-minute intervals, as depicted in Figure 13. Under a 1 h hold at fixed temperature with thermal shielding and source warm-up, the centroid-tracked wavelength exhibits a mean $\bar{\lambda} = 1546.98$ nm, standard deviation $\sigma = 0.02$ nm, peak-to-peak $\Delta\lambda_{\text{p-p}} = 0.08$ nm, and linear drift $|d\lambda/dt| < 0.05$ nm/h. These slight variations, presumably induced by ambient thermal noise, underscore the sensor's durability for extended utilization in stable environmental conditions.

No progressive degradation of the optical response was observed over the course of the three heating–cooling cycles conducted between 20 and 100 °C. However, no post-cycling microscopic, adhesion, or chemical characterization of the AZO coating was performed. Consequently, the observed spectral repeatability only demonstrates short-term optical stability and cannot conclusively exclude microscopic delamination or changes in the chemical state of the coating. Post-cycling surface microscopy and compositional analyses will be necessary to quantitatively assess the long-term structural and chemical stability of the AZO film.

After the AZO-coating procedure, the local peak-to-valley spectral contrast around 1547 nm was approximately 13.09 dB. The contrast was defined as $C_{\text{dB}} = P_{\text{max,dBm}} - P_{\text{min,dBm}}$, where $P_{\text{max,dBm}}$ and $P_{\text{min,dBm}}$ are the optical-power levels of the local maximum and its corresponding adjacent minimum within the same spectrum. The peaks, which are noted at 1547 nm, have been characterized; their positions and intensities, measured in -0.1636 dBm/°C, vary linearly with an increase in temperature with a $R^2 = 0.982$, as illustrated in Figure 14.

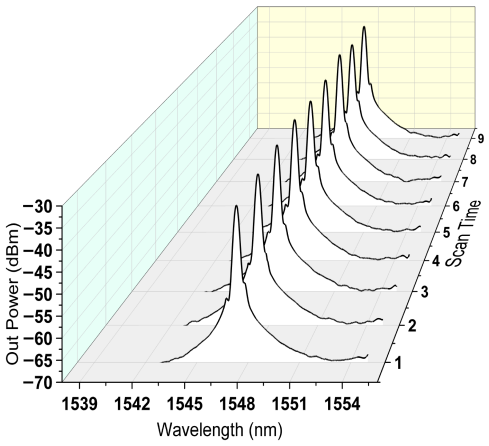


Figure 13. The stability of the sensor output over a duration of one hour.

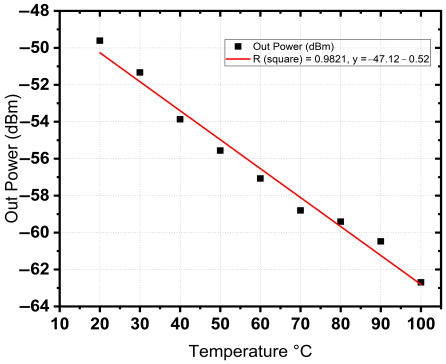


Figure 14. The output power associated with wavelength shifts at 1547 nm of the Mach–Zehnder Interferometer sensor under varying temperature conditions.

The measured wavelength temperature slope near the operating point (1547 nm) is $S_T \approx 45$ pm/°C with $R^2 > 0.99$ for a standard-SMF, non-etched, non-tapered offset-core MZI with a single AZO thin film. Beyond the slope, two aspects are critical for measurement: fringe visibility and stability, as they determine the noise-equivalent temperature (NET).

The objective of this work is not to claim a record-high temperature sensitivity, but to demonstrate a mechanically robust and reproducible core-offset Mach–Zehnder interferometer fabricated on standard single-mode fiber and functionalized with an AZO thin film. Although the achieved sensitivity of approximately 45 pm/°C in the 20–100 °C range is moderate, the device exhibits high linearity near the operating wavelength of 1547 nm, with $R^2 > 0.99$, and benefits from enhanced fringe visibility induced by the AZO coating. This improvement is relevant for practical wavelength demodulation because a higher interference contrast facilitates more reliable peak tracking. Furthermore, the fabrication route remains comparatively simple, requiring only controlled fusion-splice offsets followed by a single RF-sputtering deposition step, without grating inscription, tapering, chemical etching, or lithographic processing. Therefore, the proposed AZO-assisted core-offset MZI should be regarded as a simple, tunable, and scalable sensing platform rather than solely as a high-sensitivity temperature sensor.

While fiber Bragg gratings (FBGs) are a benchmark technology, typical temperature sensitivities in silica around 1550 nm are in the tens of pm $°C^{-1}$ and often require dedicated inscription tools and, in some cases, specific packaging to manage cross-sensitivities. Our offset-core MZI employs standard SMF and off-the-shelf splicing to create three 30 μm offsets, plus a single sputtering step for the AZO film. At the same operating wavelength (1547 nm), the AZO-coated device exhibits higher fringe visibility and a linear response of

$\sim$45 pm °C^{-1} with $R^2 > 0.99$, which we attribute to stronger cladding-mode participation. Compared with simpler offset-only interferometers, the AZO layer provides a functional route to tune coupling strength and contrast via film thickness/composition, and enables future dual-parameter operation on the same platform.

Over a continuous 1h hold at fixed temperature, the wavelength drift remained <0.1 nm, with concurrent power variations <0.5 dBm. This indicates a stable interferometric readout suitable for peak/centroid demodulation. Heating–cooling cycling (20→100→20 °C, three cycles) produced overlapping wavelength–temperature curves with linear fits that agree within their 95% confidence intervals. The point-wise scatter of the tracked peak remained within the demodulation uncertainty of the fitting routine. The discrepancy between heating and cooling paths is consistent throughout the entire 20–100 °C range, with no observable hysteresis detected for the current construction.

Discussion

The core-offset geometry provides the modal coupling and recombination required to produce the interferometric temperature response. The AZO coating modifies the boundary condition experienced by the cladding modes, and the FDTD simulations indicate stronger cladding-mode participation, higher fringe visibility, and changes in the simulated spectral response. The AZO-coated device demonstrated an experimentally determined temperature sensitivity of approximately 45 pm/°C. However, a geometrically identical uncoated device was not subjected to experimental calibration under the same temperature conditions. Consequently, the present results substantiate an enhancement in fringe visibility and spectral contrast upon incorporation of the AZO layer; however, they do not provide quantitative evidence of an improvement in temperature sensitivity relative to the uncoated core-offset configuration.

The experimental results demonstrate the efficacy of a core offset fiber sensor head in detecting variations in temperature. The sensor exhibits fluctuations and wavelength shifts observed over a 60 min period, attributed to modifications in the refractive index resulting from the aluminum-zinc coating. The refractive index of the sensor is directly affected by its temperature level, due to the composition of the medium.

The sensor operates based on the principle of wavelength demodulation, where changes in the interference spectrum result from variations in the optical path difference caused by temperature changes levels. Nonetheless, during the experimental analysis, power demodulation was employed as an ancillary approach. This technique entails observing variations in power at designated wavelengths, which correspond to changes in the interference pattern.

The core-offset configuration was selected because it can be implemented exclusively with standard SMF-28e fiber by employing controlled fusion-splice misalignment, thereby eliminating the need for cladding diameter modification or the incorporation of dissimilar fiber types. Nevertheless, no-core-fiber and SMF–MMF–SMF configurations can provide similar mode excitation and may exhibit different optical-loss and mechanical characteristics. As these alternative configurations were not subjected to experimental evaluation within the scope of the present study, no assertion is advanced regarding the superiority of the proposed structure with respect to insertion loss or mechanical robustness. A dedicated, systematic comparative investigation is still required.

A core-offset MZI can be built directly on standard single-mode fiber using only fusion splicing to introduce controlled lateral offsets; no inscription, tapering, or chemical etching is required. This preserves the full cladding diameter and therefore the mechanical robustness and ease of packaging of conventional fiber. In the presented device, an AZO thin film is incorporated as a functional layer to enhance evanescent coupling and increase

fringe visibility, thereby facilitating improved wavelength demodulation. The platform is tunable—both the offset geometry and the coating thickness/doping can be adjusted to set coupling strength and sensitivity—and it is interrogated with broadband sources without laser locking. The main limitation is that raw slope is typically lower than that of ultra-high-Q resonators, and the periodic response requires tracking across fringes.

FBGs provide a mature and compact wavelength reference with excellent linearity and compatibility with commercial interrogators and WDM multiplexing. However, they require inscription (UV or femtosecond) in suitable, often photosensitive fibers and offer limited post-fabrication tunability. Temperature measurements often necessitate specialized packaging to address cross-sensitivities to strain or pressure, and once the grating has been inscribed, enhancing sensitivity becomes challenging. For applications that emphasize minimal equipment requirements, adaptable tuning through coating applications, or the use of standard single-mode fiber without prior inscription, these limitations can be critical.

Integrated microresonators offer significant compactness and potentially exceptional sensitivity due to their large quality factors and compatibility with CMOS fabrication processes. However, they are constrained by a limited dynamic range, centered around a sharp resonance, and are susceptible to environmental drift, which frequently requires active stabilization. Additionally, challenges arise from coupling and packaging complexities encountered when interfacing chips with fiber networks. Interrogation typically relies on narrow-linewidth lasers and locking electronics, which raises system cost and complexity compared with broadband fiber-only readout.

In view of these considerations, the core-offset MZI investigated herein provides the optimal balance for a sensor that needs to be cost-effective, mechanically robust, compatible with standard SMF, and adjustable through a functional coating. The AZO-assisted design yields high-contrast fringes and a linear, stable temperature response in the C-band, while preserving a clear path to higher sensitivity and extended temperature ranges with appropriate high-temperature packaging. Moreover, the coating route naturally enables dual-parameter sensing without altering the underlying fiber platform.

The contribution of this work lies in the mechanism-supported demonstration that an AZO thin film can act as a controlled perturbation of the cladding-mode boundary condition in a standard-SMF multi-offset MZI operating in the C-band. The application of the coating modifies the effective refractive index contrast between the core-guided and cladding-guided modes, thereby altering the resulting interference fringe pattern and enhancing the robustness and precision of wavelength tracking. This effect is supported by the direct comparison between uncoated and AZO-coated configurations, where the FDTD simulations show stronger core–cladding coupling, higher fringe visibility, and a simulated FSR of approximately 3.5–3.7 nm near 1550 nm. In practical scenarios, temperature, humidity, and mechanical strain may simultaneously influence the fiber response. In the present experiments, however, the fiber was rigidly mounted on a temperature-controlled stage to effectively suppress axial strain. Consequently, the observed wavelength shifts can be predominantly ascribed to variations in temperature.

4. Conclusions

The AZO-coated core-offset MZI experimentally exhibited a temperature sensitivity of approximately 45 pm/°C over the 20–100 °C range, with $R^2 > 0.99$. This sensitivity characterizes the complete coated interferometric structure. In the absence of an experimentally calibrated, otherwise identical core-offset device without coating evaluated under the same conditions, it is not possible to ascribe any quantitatively defined enhancement in temperature sensitivity solely to the presence of the AZO layer. The FDTD comparison

instead indicates that the AZO coating modifies cladding-mode propagation and increases simulated fringe visibility and spectral contrast.

The AZO thin film investigated in this work exhibited an optical thickness of approximately 50 nm, as determined by Filmetrics measurements performed on a simultaneously coated planar witness substrate. This thickness corresponds to the specific experimental condition investigated and was not selected or validated as an optimized coating thickness.

The employment of AZO as a transparent conducting oxide not only augments the refractive index contrast between the cladding modes and the surrounding medium but also enhances the interactions of the evanescent field. These effects collectively lead to improved fringe visibility and energy redistribution, which are essential for accurate wavelength demodulation in interferometric sensors.

The proposed SMF core-offset MZI incorporating AZO exhibits a linear response over the temperature range from 20 to 100 °C, characterized by a slope of approximately 45 picometers per degree Celsius ($R^2 > 0.99$). Based on the nominal OSA wavelength resolution of 0.03 nm, the conservative temperature resolution is approximately 0.67 °C. This performance is competitive with FBGs, which exhibit changes in the range of tens of picometers per degree Celsius, without the necessity of inscription while also enabling tunable fringe contrast through coatings. In comparison to high-quality factor (high-Q) microresonators, this approach sacrifices ultimate responsivity in favor of a simpler interrogation method. The 20 to 100 °C temperature range coincides with those required for environmental and process control, thermal management in telecommunications (25–85 °C), power electronics and battery modules (20–80 °C), and common biochemical protocols (approximately 30–95 °C). AZO remains stable in neutral aqueous environments; however, for more aggressive chemical conditions, ultrathin protective layers, such as 20–50 nm of silicon dioxide (SiO_2) or parylene-C, and silanization treatments can be applied to maintain surface integrity with minimal effects on evanescent coupling.

Author Contributions: Conceptualization, R.d.J.S.-A.; data curation, M.A.R.-M. and R.d.J.S.-A.; formal analysis, M.A.R.-M. and R.d.J.S.-A.; investigation, M.A.R.-M. and S.B.-A.; methodology, M.A.R.-M.; project administration, R.d.J.S.-A. and M.G.-M.; resources, R.d.J.S.-A., M.G.-M. and J.M.S.-H.; software, M.A.R.-M.; supervision, R.d.J.S.-A.; validation, R.d.J.S.-A., M.G.-M. and J.M.S.-H.; visualization, E.G.-A., N.P.P.-R., R.C.-G., C.A.C.-A. and A.A.C.-G.; writing—original draft, M.A.R.-M. and R.d.J.S.-A.; writing—review and editing, R.d.J.S.-A., M.G.-M., and L.A. All authors have read and agreed to the published version of the manuscript.

Funding: This research received no external funding.

Data Availability Statement: The data presented in this study are available upon request from the corresponding author, and the dataset was jointly completed by the team, so the data are not publicly available.

Conflicts of Interest: The authors declare no conflicts of interest.

References

1. Perez, J.L.C.; Gutiérrez-Gutiérrez, J.; Mayoral, C.P.; Pérez-Campos, E.L.; del Socorro Pina Canseco, M.; Carrillo, L.T.; Mayoral, L.P.C.; Treviño, M.V.; Apreza, E.L.; Laguna, R.R. Fiber Optic Sensors: A Review for Glucose Measurement. *Biosensors* **2021**, *11*, 61. [CrossRef] [PubMed]
2. Palmieri, L.; Schenato, L.; Santagiustina, M.; Galtarossa, A. Rayleigh-Based Distributed Optical Fiber Sensing. *Sensors* **2022**, *22*, 6811. [CrossRef] [PubMed]
3. Tabassum, R.; Kant, R. Recent Trends in Surface Plasmon Resonance Based Fiber–Optic Gas Sensors Utilizing Metal Oxides and Carbon Nanomaterials as Functional Entities. *Sens. Actuators B Chem.* **2020**, *310*, 127813. [CrossRef]
4. Bajić, J.S.; Babić, S.; Joža, A.; Vasiljević-Toskić, M.M. Evaluation of the Fiber Optic Curvature Sensor Design Parameters for New Measurement Approach Application. *Opt. Commun.* **2024**, *570*, 130931. [CrossRef]

5. Yin, G.; Fu, Q.; Yang, P.; Zhu, T. Direction-Discriminating Torsion Sensor Based on Optical Fiber Mach–Zehnder Interferometer. *Opt. Laser Technol.* **2022**, *156*, 108461. [CrossRef]
6. Yin, G.; Xu, Z.; Ma, J.; Zhu, T. Simultaneous Measurement of Bending and Torsion in Optical Fiber Shape Sensor. *J. Light. Technol.* **2023**, *41*, 1851–1857. [CrossRef]
7. Al-dulimi, S.; Taher, H.J. High-Sensitivity Drug Biosensor Based on Taper and Offset Techniques for Coreless Optical Fiber Deposited with Titanium Dioxide Nanoparticles. *Opt. Contin.* **2024**, *3*, 589–599. [CrossRef]
8. Li, L.; Li, X.; Xie, Z.; Liao, Z.; Tu, F.; Liu, D. Simultaneous Measurement of Refractive Index and Temperature Using Thinned Fiber Based Mach–Zehnder Interferometer. *Opt. Commun.* **2012**, *285*, 3945–3949. [CrossRef]
9. Hou, Y.F.; Wang, J.; Wang, X.; Liao, Y.P.; Yang, L.; Cai, E.L.; Wang, S.S. Simultaneous Measurement of Pressure and Temperature in Seawater with PDMS Sealed Microfiber Mach–Zehnder Interferometer. *J. Light. Technol.* **2020**, *38*, 6412–6421. [CrossRef]
10. Pendão, C.; Silva, I. Optical Fiber Sensors and Sensing Networks: Overview of the Main Principles and Applications. *Sensors* **2022**, *22*, 7554. [CrossRef] [PubMed]
11. Pereira, D.; Bierlich, J.; Kobelke, J.; Ferreira, M.S. Simultaneous Measurement of Strain, Curvature, and Temperature Using a Hollow Square Core Fiber. *Opt. Laser Technol.* **2022**, *156*, 108540. [CrossRef]
12. Ma, S.; Xu, Y.; Pang, Y.; Zhao, X.; Li, Y.; Qin, Z.; Liu, Z.; Lu, P.; Bao, X. Optical Fiber Sensors for High-Temperature Monitoring: A Review. *Sensors* **2022**, *22*, 5722. [CrossRef] [PubMed]
13. Afroozeh, A. Highly Sensitive FBG-Based Sensor for Temperature Measurement Operating in Optical Fiber. *Plasmonics* **2021**, *16*, 1973–1982. [CrossRef]
14. Deng, Y.; Jiang, J. Optical Fiber Sensors in Extreme Temperature and Radiation Environments: A Review. *IEEE Sens. J.* **2022**, *22*, 13811–13834. [CrossRef]
15. Imas, J.J.; Bai, X.; Zamarreño, C.R.; Matías, I.R.; Albert, J. Accurate Compensation and Prediction of the Temperature Cross-Sensitivity of Tilted FBG Cladding Mode Resonances. *Appl. Opt.* **2023**, *62*, E8–E15. [CrossRef] [PubMed]
16. Noori, N.F.; Mansour, T.S. A Review of Recently Optical Hybrid Optical Fiber Interferometers. *J. Opt.* **2025**, *54*, 3698–3711. [CrossRef]
17. Guo, J.; Lian, S.; Zhang, Y.; Zhang, Y.; Liang, D.; Yu, Y.; Chen, R.; Du, C.; Ruan, S. High-Temperature Measurement of a Fiber Probe Sensor Based on the Michelson Interferometer. *Sensors* **2022**, *22*, 289. [CrossRef] [PubMed]
18. Riza, M.A.; Go, Y.I.; Harun, S.W.; Maier, R.R.J. FBG Sensors for Environmental and Biochemical Applications—A Review. *IEEE Sens. J.* **2020**, *20*, 7614–7627. [CrossRef]
19. Li, B.; Li, Z.; Zhang, F.; Lu, B.; Guo, P.; Guo, L.; Hou, W. A Dual-Parameter Optical Fiber Sensor Based on SPR and LMR for Measuring Liquid Refractive Index and Temperature. *IEEE Sens. J.* **2025**, *25*, 12907–12914. [CrossRef]
20. Wang, P.; Zhao, H.; Wang, X.; Farrell, G.; Brambilla, G. A Review of Multimode Interference in Tapered Optical Fibers and Related Applications. *Sensors* **2018**, *18*, 858. [CrossRef] [PubMed]
21. Qu, W.; Chen, Y.; Liu, S.; Luo, L. Advances and Prospects of Nanomaterial Coatings in Optical Fiber Sensors. *Coatings* **2025**, *15*, 1008. [CrossRef]
22. Kumar, M.D.; Park, Y.C.; Kim, J. Impact of Thin Metal Layer on the Optical and Electrical Properties of Indium-Doped-Tin Oxide and Aluminum-Doped-Zinc Oxide Layers. *Superlattices Microstruct.* **2015**, *82*, 499–506. [CrossRef]
23. Prasanth, A.; Harini, V.K.; Manivannan, P.; Narasimman, S.; Velumani, M.; Meher, S.R.; Alex, Z.C. A Comparative Study of ZnO, AZO, TiO2, Sb2O3, and SnO2 Nanomaterials Coated SPR Based Fiber Optic Refractive Index Sensors for Chemical Sensing Application. *Opt. Mater.* **2024**, *152*, 115438. [CrossRef]
24. Liang, H.; Shen, T.; Feng, Y.; Liu, H.; Han, W. A D-Shaped Photonic Crystal Fiber Refractive Index Sensor Coated with Graphene and Zinc Oxide. *Sensors* **2021**, *21*, 71. [CrossRef] [PubMed]
25. Islam, M.R.; Iftekher, A.N.M.; Noor, F.; Khan, M.R.H.; Reza, M.T.; Nishat, M.M. AZO-Coated Plasmonic PCF Nanosensor for Blood Constituent Detection in Near-Infrared and Visible Spectrum. *Appl. Phys. A* **2022**, *128*, 86. [CrossRef]
26. Henley, S.J.; Ashfold, M.N.R.; Cherns, D. The Growth of Transparent Conducting ZnO Films by Pulsed Laser Ablation. *Surf. Coat. Technol.* **2004**, *177–178*, 271–276. [CrossRef]
27. Min, R.; Liu, Z.; Pereira, L.; Yang, C.; Sui, Q.; Marques, C. Optical Fiber Sensing for Marine Environment and Marine Structural Health Monitoring: A Review. *Opt. Laser Technol.* **2021**, *140*, 107082. [CrossRef]
28. Wu, Y.; Wang, Q.; Li, Y.; Li, M.; Pan, M.; Zhou, X.; Yan, X.; Zhao, Y. A Simple High-Sensitivity Sensor Based on Multimode Mach–Zehnder Interference for Refractive Index Measurement. *IEEE Sens. J.* **2024**, *24*, 30161–30167. [CrossRef]
29. Bhardwaj, V.; Kishor, K.; Sharma, A.C. Tapered Optical Fiber Geometries and Sensing Applications Based on Mach–Zehnder Interferometer: A Review. *Opt. Fiber Technol.* **2020**, *58*, 102302. [CrossRef]
30. Zhao, R.; Shu, X.; Wang, P. High-Performance Bending Sensor Based on Femtosecond Laser-Inscribed In-Fiber Mach–Zehnder Interferometer. *J. Light. Technol.* **2020**, *38*, 6371–6378. [CrossRef]
31. Leviton, D.B.; Frey, B.J. Temperature-Dependent Absolute Refractive Index Measurements of Synthetic Fused Silica. In *Proceedings of the Optomechanical Technologies for Astronomy*; SPIE: Bellingham, WA, USA, 2006; Volume 6273, p. 62732K. [CrossRef]

32. Kersey, A.D.; Davis, M.A.; Patrick, H.J.; LeBlanc, M.; Koo, K.P.; Askins, C.G.; Putnam, M.A.; Friebele, E.J. Fiber Grating Sensors. *J. Light. Technol.* **1997**, *15*, 1442–1463. [CrossRef]
33. Saleh, B.E.A.; Teich, M.C. *Fundamentals of Photonics, 2 Volume Set*, 3rd ed.; Wiley: Hoboken, NJ, USA, 2019.
34. Prieto-Cortés, P.; Álvarez Tamayo, R.I.; García-Méndez, M.; Durán-Sánchez, M. Lossy Mode Resonance Generation on Sputtered Aluminum-Doped Zinc Oxide Thin Films Deposited on Multimode Optical Fiber Structures for Sensing Applications in the 1.55 µm Wavelength Range. *Sensors* **2019**, *19*, 4189. [CrossRef] [PubMed]
35. Ozcariz, A.; Piña-Azamar, D.A.; Zamarreño, C.R.; Dominguez, R.; Arregui, F.J. Aluminum Doped Zinc Oxide (AZO) Coated Optical Fiber LMR Refractometers—An Experimental Demonstration. *Sens. Actuators B Chem.* **2019**, *281*, 698–704. [CrossRef]
36. Yang, J.; Minn, K.; Anopchenko, A.; Gurung, S.; Lee, H.W.H. Excitation of Epsilon-Near-Zero Mode in Optical Fiber. *Laser Photonics Rev.* **2023**, *17*, 2200539. . [CrossRef]
37. Walia, K.; Verma, R.K. Lossy Mode Resonance-Based Uniform Core Tapered Fiber Optic Sensor for Sensitivity Enhancement. *Commun. Theor. Phys.* **2020**, *72*, 095502. [CrossRef]
38. Wo, J.; Wang, G.; Cui, Y.; Sun, Q.; Liang, R.; Shum, P.P.; Liu, D. Refractive Index Sensor Using Microfiber-Based Mach–Zehnder Interferometer. *Opt. Lett.* **2012**, *37*, 67–69. [CrossRef] [PubMed]
39. Luo, W.; Chen, Y.; Xu, F. Recent Progress in Microfiber-Optic Sensors. *Photonic Sens.* **2021**, *11*, 45–68. [CrossRef]
40. Zhan, X.; Liu, Y.; Tang, M.; Ma, L.; Wang, R.; Duan, L.; Gan, L.; Yang, C.; Tong, W.; Fu, S.; et al. Few-Mode Multicore Fiber Enabled Integrated Mach–Zehnder Interferometers for Temperature and Strain Discrimination. *Opt. Express* **2018**, *26*, 15332–15342. [CrossRef] [PubMed]
41. Sun, X.; Du, H.; Dong, X.; Hu, Y.; Duan, J. Simultaneous Curvature and Temperature Sensing Based on a Novel Mach–Zehnder Interferometer. *Photonic Sens.* **2020**, *10*, 171–180. [CrossRef]
42. Yin, Z.; Jing, X.; Zhang, H.; Wang, C.; Liu, C.; Shao, P. Dual-Parameter Sensor for Simultaneously Measuring Refractive Index and Temperature Based on No-Core Fiber and SPR Effect. *Optik* **2022**, *262*, 169320. [CrossRef]
43. Kumar, S.; Wang, Y.; Li, M.; Wang, Q.; Malathi, S.; Marques, C.; Singh, R.; Zhang, B. Plasmon-Based Tapered-in-Tapered Fiber Structure for p-Cresol Detection: From Human Healthcare to Aquaculture Application. *IEEE Sens. J.* **2022**, *22*, 18493–18500. [CrossRef]
44. Huerta-Mascotte, E.; Sierra-Hernandez, J.M.; Mata-Chavez, R.I.; Jauregui-Vazquez, D.; Castillo-Guzman, A.; Estudillo-Ayala, J.M.; Guzman-Chavez, A.D.; Rojas-Laguna, R. A Core-Offset Mach–Zehnder Interferometer Based on a Non-Zero Dispersion-Shifted Fiber and Its Torsion Sensing Application. *Sensors* **2016**, *16*, 856. [CrossRef] [PubMed]
45. Yadav, R.P.; Rai, K.B.; Shrestha, S.P. Electrical and Optical Properties of Dip Coated Al-Doped ZnO Thin Films: Effect of Al-Concentration, Starting Solution and Sample Ageing. *Mong. J. Chem.* **2021**, *22*, 38–44. [CrossRef]
46. Huang, J.H.; Tan, R.Q.; Li, J.; Zhang, Y.L.; Yang, Y.; Song, W.J. Thermal Stability of Aluminum Doped Zinc Oxide Thin Films. *Mater. Sci. Forum* **2011**, *685*, 147–151. [CrossRef]
47. Murali, A.; Sohn, H.Y.; Sarswat, P.K. Plasma-Assisted Chemical Vapor Synthesis of Aluminum-Doped Zinc Oxide Nanopowder and Synthesis of AZO Films for Optoelectronic Applications. *J. Electron. Mater.* **2019**, *48*, 2531–2542. [CrossRef]
48. Ma, S.; Zhang, Y.; Qiu, H.; Zhao, C.; Hu, X.; Qu, H. Fiber Optic Mach–Zehnder Temperature Sensor Based on Dual-Core Fiber. In *Proceedings of the European Workshop on Optical Fibre Sensors (EWOFS) 2023*; SPIE: Bellingham, WA, USA, 2023; Volume 12643, pp. 69–72. [CrossRef]
49. Raha, S.; Ahmaruzzaman, M. ZnO nanostructured materials and their potential applications: Progress, challenges and perspectives. *Nanoscale Adv.* **2022**, *4*, 1868–1925. [CrossRef] [PubMed]
50. Jimenez-Gonzalez, A.E.; Soto Urueta, J.A.; Suarez-Parra, R. Optical and electrical characteristics of aluminum-doped ZnO thin films prepared by solgel technique. *J. Cryst. Growth* **1998**, *192*, 430–438. [CrossRef]
51. Znaidi, L. Sol–gel-deposited ZnO thin films: A review. *Mater. Sci. Eng. B* **2010**, *174*, 18–30. [CrossRef]
52. Badgujar, A.C.; Yadav, B.S.; Jha, G.K.; Dhage, S.R. Room Temperature Sputtered Aluminum-Doped ZnO Thin Film Transparent Electrode for Application in Solar Cells and for Low-Band-Gap Optoelectronic Devices. *ACS Omega* **2022**, *7*, 14203–14210. [CrossRef] [PubMed]
53. Regmi, G.; Rijal, S.; Velumani, S. Aluminum-doped zinc oxide (AZO) ultra-thin films deposited by radio frequency sputtering for flexible Cu (In, Ga) Se2 solar cells. *Mem.-Devices Circuits Syst.* **2023**, *5*, 100064. [CrossRef]
54. Prieto-Cortés, P.; Álvarez-Tamayo, R.; García-Méndez, M.; Durán-Sánchez, M.; Barcelata-Pinzón, A.; Ibarra-Escamilla, B. Magnetron sputtered Al-doped ZnO thin film as saturable absorber for passively Q-switched Er/Yb double clad fiber laser. *Laser Phys. Lett.* **2019**, *16*, 045101. [CrossRef]
55. Wang, H.; Zheng, L.; Zhang, J.; Liu, J. Orientation-dependent fiber-optic inclinometer based on misalignment-spliced structure. *Sci. Rep.* **2022**, *12*, 9225. [CrossRef] [PubMed]
56. Li, X.; et al. Temperature-insensitive liquid level sensor based on a U-shaped cascade core-offset structure. *Appl. Opt.* **2024**, *64*, 115–123. [CrossRef] [PubMed]

57. Aydin, D.; Barnes, J.A.; Loock, H.P. In-Fiber Interferometry Sensors for Refractive Index. *Appl. Phys. Rev.* **2023**, *10*, 011307. [CrossRef]
58. Rakić, A.D.; Djurišić, A.B.; Elazar, J.M.; Majewski, M.L. Optical Properties of Metallic Films for Vertical-Cavity Optoelectronic Devices. *Appl. Opt.* **1998**, *37*, 5271–5283. [CrossRef] [PubMed]
59. Toan, N.V.; Tuoi, T.T.K.; Inomata, N.; Toda, M.; Ono, T. Aluminum Doped Zinc Oxide Deposited by Atomic Layer Deposition and Its Applications to Micro/Nano Devices. *Sci. Rep.* **2021**, *11*, 1204. [CrossRef] [PubMed]
60. Riley, C.T.; Kieu, T.A.; Smalley, J.S.T.; Pan, S.H.A.; Kim, S.J.; Post, K.W.; Kargar, A.; Basov, D.N.; Pan, X.; Fainman, Y.; et al. Plasmonic Tuning of Aluminum-Doped Zinc Oxide Nanostructures by Atomic Layer Deposition. *Phys. Status Solidi RRL* **2014**, *8*, 948–952. [CrossRef]
61. Naik, G.V.; Liu, J.; Kildishev, A.V.; Shalaev, V.M.; Boltasseva, A. Demonstration of Al:ZnO as a Plasmonic Component for Near-Infrared Metamaterials. *Proc. Natl. Acad. Sci. USA* **2012**, *109*, 8834–8838. [CrossRef] [PubMed]
62. Guillén, C.; Trigo, J.F. Ellipsometric Study on the Uniformity of Al:ZnO Thin Films Deposited Using DC Sputtering at Room Temperature over Large Areas. *Materials* **2023**, *16*, 6644. [CrossRef] [PubMed]
63. Lu, P.; Men, L.; Sooley, K.; Chen, Q. Tapered Fiber Mach–Zehnder Interferometer for Simultaneous Measurement of Refractive Index and Temperature. *Appl. Phys. Lett.* **2009**, *94*, 131110. [CrossRef]
64. Zhou, Y.; Liu, Y.; Zheng, J. Investigation of an Inline Fiber Mach–Zehnder Interferometer Based on Hybrid Joints of Core-Offset and Peanut-Shape for Refractive Index Sensing. *Opt. Fiber Technol.* **2023**, *81*, 103521. [CrossRef]

Disclaimer/Publisher's Note: The statements, opinions and data contained in all publications are solely those of the individual author(s) and contributor(s) and not of MDPI and/or the editor(s). MDPI and/or the editor(s) disclaim responsibility for any injury to people or property resulting from any ideas, methods, instructions or products referred to in the content.